Effects of Roughness Length Parameterizations on Regional-Scale Land Surface Modeling of Alpine Grasslands in the Yangtze River Basin

YING HUANG

Faculty of Geo-Information Science and Earth Observation, and Faculty of Engineering Technology, University of Twente, Enschede, Netherlands

M. SUHYB SALAMA, ZHONGBO SU, AND ROGIER VAN DER VELDE

Faculty of Geo-Information Science and Earth Observation, University of Twente, Enschede, Netherlands

DONGHAI ZHENG

Faculty of Geo-Information Science and Earth Observation, and Faculty of Engineering Technology, University of Twente, Enschede, Netherlands

MAARTEN S. KROL AND ARJEN Y. HOEKSTRA

Faculty of Engineering Technology, University of Twente, Enschede, Netherlands

YUNXUAN ZHOU

State Key Laboratory of Estuarine and Coastal Research, East China Normal University, Shanghai, China

(Manuscript received 1 April 2015, in final form 2 December 2015)

ABSTRACT

Current land surface models (LSMs) tend to largely underestimate the daytime land surface temperature T_{sfc} for high-altitude regions. This is partly because of underestimation of heat transfer resistance, which may be resolved through adequate parameterization of roughness lengths for momentum z_{0m} and heat z_{0h} transfer. In this paper, the regional-scale effects of the roughness length parameterizations for alpine grasslands are addressed and the performance of the Noah LSM using the updated roughness lengths compared to the original ones is assessed. The simulations were verified with various satellite products and validated with ground-based observations. More specifically, four experimental setups were designed using two roughness length schemes with two different parameterizations of z_{0m} (original and updated). These experiments were conducted in the source region of the Yangtze River during the period 2005–10 using the Noah LSM. The results show that the updated parameterizations of roughness lengths reduce the mean biases of the simulated daytime T_{sfc} in spring, autumn, and winter by up to 2.7 K, whereas larger warm biases are produced in summer. Moreover, model efficiency coefficients (Nash–Sutcliffe) of the monthly runoff results are improved by up to 26.3% when using the updated roughness parameterizations. In addition, the spatial effects of the roughness length parameterizations on the T_{sfc} simulations are discussed. This study stresses the importance of proper parameterizations of z_{0m} and z_{0h} for LSMs and highlights the need for regional adaptation of the z_{0m} and z_{0h} values.

1. Introduction

The Tibetan Plateau is geographically known as the roof of the world or third pole of the earth. It not only plays an important role in the formation of the Asian monsoon (Yanai et al. 1992; Yanai and Wu 2006), but it also serves as the headwaters of several large rivers in East and Southeast Asia, such as the Indus, Mekong, Brahmaputra, Yellow, and Yangtze Rivers. This area has experienced significant environmental changes, such as increased warming (e.g., Chen and Frauenfeld 2014), enhanced frequency of drought (e.g., Ma and Fu 2006), intensified land degradation, and desertification (e.g., Fu and Wen 2002). In addition, Immerzeel et al. (2010) have shown that the hydrologic cycle has changed in recent years, influencing runoff of rivers originating from the region. Reliable hydrometeorological

Corresponding author address: Ying Huang, Faculty of Geo-Information Science and Earth Observation, University of Twente, P.O. Box 217, 7500 AE Enschede, Netherlands.
E-mail: yinghuangje@gmail.com

DOI: 10.1175/JHM-D-15-0049.1

simulations are required assets for understanding land–atmosphere interactions on the Tibetan Plateau and their response to climate change and human activities.

The Tibetan Plateau is an arid and semiarid region mainly characterized by bare soil and grassland. Because of strong solar radiation, low air density, and the influence of the Asian monsoon, the Tibetan Plateau has very distinct and complex diurnal and seasonal variations of the surface energy and water budget (Yang et al. 2009). Because of this, current land surface models (LSMs), for example, Community Land Model (CLM); Simple Biosphere Model, version 2 (SiB2); and Noah LSM, tend to significantly underestimate the daytime land surface temperature T_{sfc} and overestimate sensible heat flux H on the Tibetan Plateau, particularly in dry conditions (Yang et al. 2007, 2009; Chen et al. 2011).

In these LSMs, the bulk formulations based on the Monin–Obukhov similarity theory (MOST) have usually been employed to simulate the surface heat fluxes between the land surface and atmosphere (Garratt 1994; Brutsaert 1998; Su et al. 2001). Su et al. (2001) have documented that, in order to accurately reproduce H through MOST, the roughness lengths for momentum z_{0m} and heat z_{0h} transfer must be determined properly. Both parameters cannot be directly measured, but they can be ideally determined using the bulk transfer equations from profile measurements of wind and temperature (Sun 1999; Ma et al. 2002; Yang et al. 2003) and/or from single-level sonic anemometer measurement (Sun 1999; Martano 2000; Ma et al. 2008). The importance of z_{0m} and z_{0h} to LSMs has been reported by many authors. For instance, LeMone et al. (2008) have pointed out that a proper representation of z_{0h} is helpful to reproduce the observed T_{sfc} and H. Yang et al. (2009) have further confirmed that the underestimation of heat transfer resistances accounts for the daytime T_{sfc} underestimation in current LSMs for the Tibetan Plateau. Based on these results, we argue that robust parameterizations of z_{0m} and z_{0h} are imperative for reliable surface heat flux estimates and T_{sfc} calculation on the Tibetan Plateau.

There are a number of theoretical and experimental studies on the parameterizations of z_{0m} and z_{0h} for LSMs. In general, z_{0m} is estimated according to surface canopy characteristics, whereas z_{0h} is calculated based on z_{0m} through the parameterizations of kB^{-1} [$kB^{-1} = \ln(z_{0m}/z_{0h})$]. Brutsaert (1982, hereafter B82) combined the roughness Reynolds number Re* and vegetation characteristics (e.g., leaf area index and canopy height) to parameterize kB^{-1}. Zilitinkevich (1995, hereafter Z95) proposed an empirical coefficient, known as the Zilitinkevich empirical coefficient C_{Zil}, to relate Re* to kB^{-1}, and since Chen et al. (1997), Z95 has been widely used in LSMs. Chen and Zhang (2009, hereafter C09) found that the z_{0m} and z_{0h} of Z95 tend to be overestimated for short vegetation and underestimated for tall vegetation, and hence, on the basis of Z95, parameterized z_{0m} and z_{0h} as functions of canopy height. Similarly, Zheng et al. (2012, hereafter Z12) proposed to utilize green vegetation fraction (GVF) for the modification of Z95. In addition, Yang et al. (2008, hereafter Y08) assessed several schemes, including B82 and Z95, and showed that z_{0m} and z_{0h} can be more realistically parameterized by taking into account friction velocity u_* and friction temperature θ_* in arid and semiarid regions of China.

For the Tibetan Plateau, on the other hand, the studies on roughness length parameterizations were still very limited until 1998, when intensive field experiments and comprehensive observational networks started to develop (Koike 2004; Ma et al. 2008; Xu et al. 2008). Since then, a number of progresses have been made in the parameterizations of roughness lengths for the Tibetan Plateau. For instance, Chen et al. (2010) showed that Y08 can perform better on the Tibetan Plateau based on extensive evaluation of different roughness length schemes in LSMs. This study is very valuable, but it is limited to 2-month premonsoon episodes and did not consider revising roughness length schemes other than Y08 to operate on the Tibetan Plateau. This kind of revision was performed by Zheng et al. (2014), in which they used field measurements to revise the values of z_{0m} for Z95, C09, and Z12 for a Tibetan site in different seasons. Zheng et al. (2014) showed that revising the values for z_{0m} and z_{0h} dramatically improves the performance of the Noah LSM on the simulations of T_{sfc} and surface heat fluxes at a point scale, and they suggested using C09 with the newly revised z_{0m} for actual application because of its consistent performance in different seasons.

The impacts of roughness length parameterizations on T_{sfc} and surface heat fluxes, as well as water fluxes simulations at a regional scale, are yet to be investigated for the Tibetan Plateau. In this study, we extend on the previous study of Zheng et al. (2014) by assessing parameterizations of roughness lengths for T_{sfc} and heat fluxes estimation at a regional scale for the Tibetan Plateau. Furthermore, we explore their effects on the simulations of water fluxes and states. We selected two roughness length parameterization schemes, Z95 and C09, with the original and the Zheng et al. (2014)–derived roughness lengths for evaluation. Our selection was based on the common usage of Z95 in LSMs, whereas C09 has better performance than Y08 and Z12 (Zheng et al. 2014). Moreover, the Jinsha, Mintuo, and Jialing subbasins (the source region) of the Yangtze

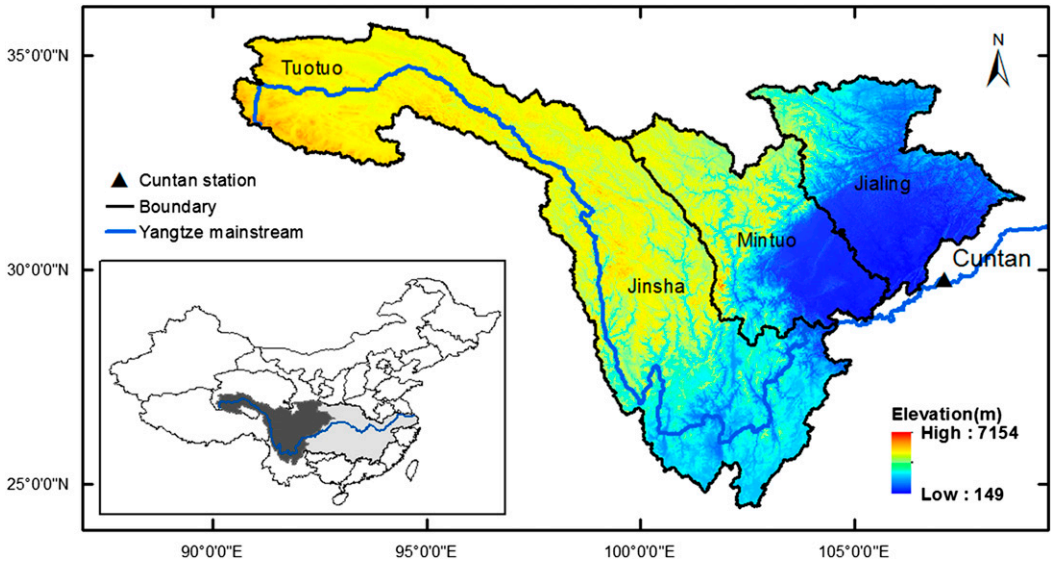

FIG. 1. Elevation map of the Jinsha, Mintuo, and Jialing subbasins located in the upper reaches of the Yangtze. The black triangle represents the Cuntan hydrological station. The main stream of the Yangtze is delineated in blue, and the boundary of the three subbasins is in black.

River are taken as the study area (Fig. 1). This is mainly because the source region of the Yangtze River has diverse hydrometeorological conditions and is relatively less influenced by human activities than the neighboring catchments, such as the source region of the Yellow River basin.

This paper is organized as follows. First, we introduce the Noah LSM and the two roughness length schemes, Z95 and C09, in section 2. Section 3 provides a description of the study area and the datasets used. In section 4, we give detailed explanations of four experiments that were designed to evaluate different roughness length parameterizations. The simulated T_{sfc}, runoff, and terrestrial water storage (TWS) changes are evaluated in section 5, and the results are verified and discussed in section 6. Finally, the conclusions are drawn in section 7.

2. Noah land surface model

The Noah LSM has been widely used for surface heat flux and hydrology simulations, and it forms the land component of mesoscale and global weather forecasting models for investigating complex interactions between land and atmosphere (Dirmeyer et al. 2006; Zhang et al. 2011). It uses a Penman-based approximation for latent heat flux (LE) to solve surface energy balance (Mahrt and Ek 1984), a four-layer soil model with thermal conduction equations for simulating the soil heat transport, and the diffusivity form of Richards's equation for soil water movement (Mahrt and Pan 1984). A simple water balance (SWB) model is used by the Noah LSM to calculate the surface runoff (Schaake et al. 1996).

a. Surface energy budget

In general, the surface energy balance equation can be written as

$$R_{net} = (1-\alpha)S^{\downarrow} + \varepsilon(L^{\downarrow} - \sigma T_{sfc}^4) \quad \text{and} \tag{1}$$

$$R_{net} = H + \mathrm{LE} + G_0. \tag{2}$$

In Eq. (1), R_{net} is the net radiation ($\mathrm{W\,m^{-2}}$) and $S^{\downarrow}$ and $L^{\downarrow}$ are the downward shortwave and longwave radiation ($\mathrm{W\,m^{-2}}$), respectively. The variable T_{sfc} is the land surface temperature (K), σ is the Stefan–Boltzmann constant ($5.67 \times 10^{-8}\,\mathrm{W\,m^{-2}\,K^{-4}}$), α is the surface albedo (unitless), and ε is the surface emissivity (unitless). In Eq. (2), H is the sensible heat flux ($\mathrm{W\,m^{-2}}$), LE is the latent heat flux ($\mathrm{W\,m^{-2}}$), and G_0 is the soil heat flux ($\mathrm{W\,m^{-2}}$).

The sensible heat flux is calculated through the bulk heat transfer equation based on the MOST (Garratt 1994; Brutsaert 1998):

$$H = -\rho c_p C_h u(\theta_{air} - \theta_{sfc}), \tag{3}$$

where ρ is the air density ($\mathrm{kg\,m^{-3}}$), c_p is the specific heat capacity of dry air ($1005\,\mathrm{J\,kg^{-1}\,K^{-1}}$), C_h is the land–atmosphere exchange coefficient for heat (unitless), u is the wind speed ($\mathrm{m\,s^{-1}}$), θ_{air} is the potential air temperature (K), and θ_{sfc} is the potential temperature

at the surface (K). It is worth noting that C_h is calculated based on the roughness lengths, which will be introduced later.

In the Noah LSM, the potential evaporation LE_P is calculated using a Penman-based energy balance approach (Mahrt and Ek 1984). The derivation of LE_P imposes a saturated ground surface and zero canopy resistance while combining a bulk aerodynamic formulation with a surface energy balance expression to yield a diurnally varying LE_P. The diurnally dependent LE_P can be written as

$$\mathrm{LE}_P = \frac{\Delta(R_{\mathrm{net}} - G_0) + \rho\lambda C_q u(q_s - q)}{1 + \Delta}, \tag{4}$$

where Δ is the slope of the saturated vapor pressure curve ($\mathrm{kPa\,K^{-1}}$); λ is the latent heat of vaporization ($\mathrm{J\,kg^{-1}}$); C_q is the exchange coefficient for water vapor; and q_s and q are the saturation and actual specific humidity ($\mathrm{kg\,kg^{-1}}$) at the first atmospheric model level, respectively. It is worth noting that C_q is assumed to be the same as C_h and calculated based on the roughness lengths, which will be introduced later.

The actual evapotranspiration (ET) is calculated as the sum of three components, which are soil evaporation E_{dir}, evaporation of intercepted precipitation by the canopy E_c, and transpiration through the stomata of the vegetation E_t. The soil evaporation extracted from the top soil layer is calculated as

$$E_{\mathrm{dir}} = (1 - f_c)\left(\frac{\theta_1 - \theta_w}{\theta_s - \theta_w}\right)^{\mathrm{fx}} \mathrm{LE}_P, \tag{5}$$

where f_c is the fractional vegetation cover, fx is an empirical constant taken equal to 2.0, θ_s is the saturated soil moisture content, θ_w is the soil moisture content at wilting point, and θ_1 is the soil moisture content in the first soil layer ($\mathrm{m^3\,m^{-3}}$).

The direct evaporation of rain intercepted by the canopy is calculated as

$$E_c = f_c \mathrm{LE}_P \left(\frac{\mathrm{cmc}}{\mathrm{cmc}_{\mathrm{max}}}\right)^{0.5}, \tag{6}$$

where cmc and $\mathrm{cmc}_{\mathrm{max}}$ are the actual and maximum canopy moisture contents ($\mathrm{kg\,m^{-2}}$), respectively.

Moreover, the evaporation from the root zone through the stomata, often referred to as transpiration, is determined following

$$E_t = f_c P_c \mathrm{LE}_P \left[1 - \left(\frac{\mathrm{cmc}}{\mathrm{cmc}_{\mathrm{max}}}\right)^{0.5}\right], \tag{7}$$

where P_c is the plant coefficient.

The soil heat flux is calculated following Fourier's Law using the temperature gradient between the surface and the midpoint of the first soil layer:

$$G_0 = K_h(\theta)\frac{\partial(T)}{\partial(Z)} = K_h(\theta)\frac{T_{\mathrm{sfc}} - T_{s_1}}{dz}, \tag{8}$$

where T_{s_1} is the temperature at the midpoint of the first soil layer (K), Z is the depth below the soil surface, and K_h is the soil thermal conductivity ($\mathrm{W\,m^{-1}\,K^{-1}}$) that is a function of soil water content θ and soil properties.

b. Runoff simulation and water budget

The Noah surface infiltration scheme follows an SWB model (Schaake et al. 1996) for its treatment of the subgrid variability of precipitation and soil moisture. Surface water is generated when the rain intensity exceeds the infiltration capacity and is calculated as

$$R_{\mathrm{surf}} = P - I_{\mathrm{max}}, \tag{9}$$

where R_{surf} is the surface runoff ($\mathrm{m\,s^{-1}}$), P is the rain intensity ($\mathrm{m\,s^{-1}}$), and I_{max} is the maximum infiltration capacity ($\mathrm{m\,s^{-1}}$).

Maximum infiltration capacity can be written as

$$I_{\mathrm{max}} = P\frac{D_b[1 - \exp(\mathrm{kdt})]}{P + D_b[1 - \exp(\mathrm{kdt})]}, \tag{10}$$

where D_b is the total soil moisture deficit in the soil column ($\mathrm{m^3\,m^{-3}}$) and kdt is a constant (unitless) defined by

$$\mathrm{kdt} = \mathrm{kdt}_{\mathrm{ref}}\frac{K_s}{K_{\mathrm{ref}}}, \tag{11}$$

where K_s is the saturated hydraulic conductivity ($\mathrm{m\,s^{-1}}$) and $\mathrm{kdt}_{\mathrm{ref}}$ and K_{ref} are experimentally determined parameters set to 3.0 (unitless) and 2.0×10^{-6} ($\mathrm{m\,s^{-1}}$) for large-scale simulations, respectively.

The base flow is calculated as follows:

$$R_{\mathrm{base}} = \mathrm{SLOPE}[K(\theta_4)], \tag{12}$$

where K is the hydraulic conductivity ($\mathrm{m\,s^{-1}}$), θ_4 is the moisture content in the fourth soil layer, and SLOPE is the slope coefficient (unitless).

The water balance equation can be written as

$$P = Q + \mathrm{ET} + \Delta S \quad \text{and} \tag{13}$$

$$Q = R_{\mathrm{surf}} + R_{\mathrm{base}}, \tag{14}$$

TABLE 1. Experiments with different parameterizations of z_{0m} and z_{0h} (m) implemented in the Noah LSM. Values of z_{0h} are calculated based on z_{0m} and the formulation is $z_{0h} = z_{0m}\exp(-\kappa C_{\mathrm{Zil}}\sqrt{\mathrm{Re}^*})$ with $\mathrm{Re}^* = u_* z_{0m}/\nu$, where C_{Zil} is the Z95 empirical coefficient, Re* is the roughness Reynolds number, u_* is the friction velocity ($\mathrm{m\,s^{-1}}$), ν is the kinematic molecular viscosity (taken as $1.5 \times 10^{-5}\,\mathrm{m^2\,s^{-1}}$), and $\mathrm{GVF_{norm}} = (\mathrm{GVF} - \mathrm{GVF_{min}})/(\mathrm{GVF_{max}} - \mathrm{GVF_{min}})$.

	Scheme	C_{Zil}	z_{0m} for grassland (m)	Reference
Z95-original	Z95	0.1	0.120	Z95
Z95-updated	Z95	0.1	0.035	Z95; Zheng et al. (2014)
C09-original	C09	$10^{-0.4z_{0m}/0.07}$	$(1-\mathrm{GVF_{norm}})z_{0m,\min} + (\mathrm{GVF_{norm}})z_{0m,\max}$; $z_{0m,\min} = 0.100$, $z_{0m,\max} = 0.120$	C09
C09-updated	C09	$10^{-0.4z_{0m}/0.07}$	$(1-\mathrm{GVF_{norm}})z_{0m,\min} + (\mathrm{GVF_{norm}})z_{0m,\max}$; $z_{0m,\min} = 0.011$, $z_{0m,\max} = 0.035$	C09; Zheng et al. (2014)

where Q is the runoff ($\mathrm{m\,s^{-1}}$), ET is the evapotranspiration ($\mathrm{m\,s^{-1}}$), and ΔS ($\mathrm{m\,s^{-1}}$) is the change in water storage.

c. *Roughness length parameterizations for the Noah LSM*

Z95 and C09 are two roughness length schemes that are currently utilized within the Noah LSM, and their formulations are shown in Table 1. In the scheme Z95, z_{0m} is defined as a function of land cover, and the Reynolds number–dependent formulation proposed by Z95 is implemented for the z_{0h} calculation. The Zilitinkevich empirical coefficient is a constant and currently specified as 0.1 in the Noah LSM based on calibration with field data measured over grassland (Chen et al. 1997). As can be seen from Table 1, C_{Zil} is a key parameter for z_{0h} calculation. However, C09 found that the parameterization of C_{Zil} in Z95 is unable to reproduce the seasonal variations of z_{0h} because of plant growth pattern, and they proposed to relate C_{Zil} to canopy height. Therefore, in the scheme C09, C_{Zil} was calculated based on z_{0m} ($C_{\mathrm{Zil}} = 10^{-0.4z_{0m}/0.07}$), whereas the seasonal values of z_{0m} were calculated based on GVF (Table 1). More specifically, the values of z_{0m} for grassland in C09 are linearly interpolated between a minimum $z_{0m,\min}$ (equal to bare soil z_{0m} when GVF = 0) and a maximum $z_{0m,\max}$ (equal to fully vegetated z_{0m} when GVF = 1). This modification is based on a relationship derived from 12 AmeriFlux datasets collected over a variety of land covers and climate regimes.

The surface exchange coefficient for heat and water vapor transfers are parameterized as functions of roughness lengths by Chen et al. (1997) as follows:

$$C_h = C_q = \frac{\kappa^2/R}{\left[\ln\left(\frac{z}{z_{0m}}\right) - \Psi_m\left(\frac{z}{L}\right) + \Psi_m\left(\frac{z_{0m}}{L}\right)\right]\left[\ln\left(\frac{z}{z_{0h}}\right) - \Psi_h\left(\frac{z}{L}\right) + \Psi_h\left(\frac{z_{0h}}{L}\right)\right]}, \tag{15}$$

where z_{0m} is the roughness length for momentum transport (m); z_{0h} is the roughness length for heat transport; Ψ_m and Ψ_h are the stability correction function for momentum and sensible heat transfer, respectively; L is the Obukhov length (m); z is the observation height (m); κ is the von Kármán constant (taken as 0.4); and R is related to the turbulent Prandtl number (Pr) and is taken as 1.0.

d. *Implementation*

In this study, we employed the Noah LSM, version 3.4.1, which is freely available online (http://www.ral.ucar.edu/research/land/technology/lsm.php). The U.S. Geological Survey (USGS) 30-s global 24-category vegetation (land use) data were used as the land-use data. The corresponding vegetation parameters and soil hydraulic and thermal parameters are obtained from the default database of the Noah LSM. The monthly GVF database for the Noah LSM is based on the 5-yr (1985–90) Advanced Very High Resolution Radiometer (AVHRR) normalized difference vegetation index (NDVI) products. Four soil layers with thicknesses of 0.1, 0.3, 0.6, and 1.0 m are prescribed by the application of Noah in a default mode. The spinup was completed by running the model repeatedly through 2004 until each of the variables, which include T_{sfc}, runoff, and soil moisture, reaches equilibrium, when each of the variables for the spinup in the nth year meets the condition of the following equation:

$$|\mathrm{Var}^n - \mathrm{Var}^{n-1}| < 0.001|\mathrm{Var}^{n-1}|,$$

where Var stands for each of the variables for the spinup and n is the year number.

3. Study area and datasets

a. *Description of the study area*

The Jinsha, Mintuo, and Jialing subbasins in the upper reaches of the Yangtze, located in the central and

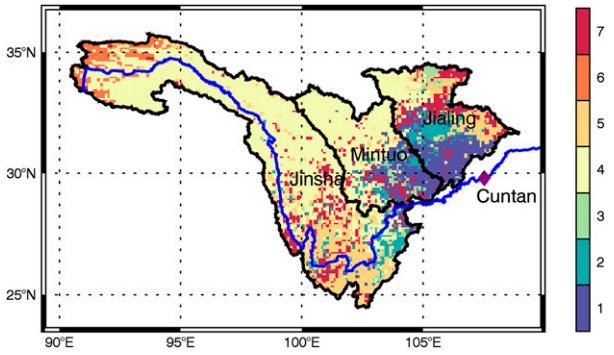

FIG. 2. The distribution of vegetation based on the USGS land-cover classification. The classes 1–7 represent the land covers of dryland cropland and pasture (1), irrigated cropland and pasture (2), cropland/grassland mosaic (3), grassland (4), shrubland (5), mixed shrubland/grassland (6), and other (7). It is noted that class 4 represents the land cover of grassland.

eastern part of the Tibetan Plateau, are the study area. As shown in Fig. 1, the source region of the Yangtze River lies in a high-altitude mountainous area. The Tuotuo River is the source of the Yangtze River and originates from the glaciers of the Jianggendiru Snow Mountains in the Tanggula mountain range.

The climate in the study area is governed by the East Asian monsoon. As a result, it has a large southeast–northwest precipitation gradient, and the annual precipitation (rainfall and snowfall) amount within the study area tends to decrease inland. The annual precipitation amount is about 400 mm yr^{-1}, 85% of which occurs during the wet/warm season from May to October. This is a specific weather phenomenon of the Yangtze River basin. Under the unique plateau climate, the land cover of the study area mainly consists of grasslands (Fig. 2). More specifically, these alpine grasslands vary from semiarid steppe and shrublands to alpine steppe and moist alpine meadows, which are closely associated with the precipitation gradient across the plateau.

b. *Discharge observations*

The Cuntan gauging station (29.77°N, 107.1°E) is located along the mainstream of the Yangtze and receives discharge from catchment areas of 0.86×10^6 km^2, which includes the study area (Fig. 1). The monthly measured discharge data of Cuntan station for the period of 2005–10 were used to examine the runoff estimation of the designed numerical experiments. These data have been collected and accumulated by the daily discharge data of the Cuntan hydrological gauging station (available at http://219.140.196.71/sq/data/sc.action?scid=cjh.sq). The regional accuracy of the Noah runoff output is assessed by comparing the spatially averaged time series of runoff in the study area to the corresponding time series generated from the observed discharge at the Cuntan gauging station for the study period. The procedure of computing the spatially averaged time series of runoff is based on the method of Balsamo et al. (2009) and is implemented as follows. First, the discharge data ($m^3 s^{-1}$) of the Cuntan station are accumulated to monthly discharge (m^3 $month^{-1}$) and divided by the area of the study area, because the Cuntan gauging station is the outlet of the study area. Second, the daily runoff data simulated by the Noah LSM are accumulated to monthly values at each pixel during the study period. The spatially averaged time series of Noah runoff is then computed as the spatial mean of these accumulated monthly values of all pixels located in the study area.

The observed discharge data of the Cuntan station are barely influenced by significant aquifers operation or other human activities, as human activities mainly occur in the middle and lower reaches of the basin. More specifically, the Three Gorges Reservoir (TGR) has little influence on the discharge of the Cuntan station, as Cuntan forms the entrance to the TGR (Yang et al. 2010). According to the Global Map of Irrigation Areas (GMIA) provided by the global water information system (AQUASTAT) of the Food and Agriculture Organization of the United Nations (FAO), the minority of irrigation occurs in the source region of the basin. Thus, the observed discharge of the Cuntan station is also not much affected by irrigation. In addition, the population in the source region of the basin is small, and therefore the effects of human water use on the observed discharge of the Cuntan station can be negligible.

c. *Atmospheric forcing*

The Institute of Tibetan Plateau Research, Chinese Academy of Sciences (hereafter ITPCAS) provides an atmospheric forcing dataset for China (He and Yang 2011). The ITPCAS forcing data merged the observations collected at 740 operational stations of the China Meteorological Administration (CMA) to the corresponding Princeton meteorological forcing data (Sheffield et al. 2006), producing near-surface air temperature, pressure, wind speed, and specific humidity. The precipitation field has been produced by combining three precipitation datasets, including precipitation observations from 740 operational stations, the Tropical Rainfall Measuring Mission (TRMM) 3B42 precipitation products (Huffman et al. 2007), and the Global Land Data Assimilation System (GLDAS) precipitation data. The Global Energy and Water Cycle Experiment–surface radiation budget (GEWEX-SRB) shortwave radiation data and Princeton forcing data

were combined and corrected by radiation estimates from CMA station data using a hybrid radiation model (Yang et al. 2006) to produce downward shortwave radiation. Based on the produced near-surface air temperature, pressure, specific humidity, and downward shortwave radiation, the downward longwave radiation is calculated by the model of Crawford and Duchon (1999). The temporal and spatial resolutions of the ITPCAS forcing data are 3 hourly and 0.1°, respectively. This dataset can be obtained online (http://westdc.westgis.ac.cn/data/7a35329c-c53f-4267-aa07-e0037d913a21).

d. MODIS land surface temperature

Moderate Resolution Imaging Spectroradiometer (MODIS) T_{sfc} products (LPDAAC 2001) were used as the ground "reference" to evaluate the T_{sfc} modeling. The MODIS/*Terra* T_{sfc} and Emissivity Daily Level 3 Global 0.05° Climate Modeling Grid (MOD11C1) products provide T_{sfc} two times per day, in the daytime around 1030 local standard time (LST) and in the nighttime around 2230 LST. In this study, we selected 312 daytime cloud-free MODIS images from the MOD11C1 T_{sfc} product archive, covering the period 2005–10. Our choice of daytime T_{sfc} product is supported by the fact that parameterization of roughness lengths plays a more important role in the daytime T_{sfc} simulation than in the nighttime one (Chen et al. 2011). MODIS data are freely available online (https://lpdaac.usgs.gov/dataset_discovery/modis/modis_products_table).

e. GRACE

Gravity Recovery and Climate Experiment (GRACE) land products, with the spatial resolution of 1°, were used in this study to validate the Noah LSM–simulated monthly TWS changes (Swenson 2012). The data are based on the Release-05 (RL05) spherical harmonics from the Center for Space Research (CSR; University of Texas at Austin, United States), the Jet Propulsion Laboratory (JPL; NASA, United States), and the German Research Centre for Geosciences (GFZ; Potsdam, Germany). The additional postprocessing steps (Swenson and Wahr 2006; Landerer and Swenson 2012) are summarized online (http://grace.jpl.nasa.gov/data/get-data/monthly-mass-grids-land/). We used the GRACE data processed by CSR during the period 2005–10, which can be freely downloaded (ftp://podaac-ftp.jpl.nasa.gov/allData/tellus/L3/land_mass/RL05/netcdf/).

4. Experiments design

To assess the effects of roughness length parameterizations on the Noah LSM simulations, we designed four numerical experiments with different configurations, that is, Z95-original, Z95-updated, C09-original, and C09-updated (Table 1). These four experiments were conducted for the study area during the period 2005–10. The first two experiments, Z95-original and Z95-updated, employ the Z95 scheme, whereas C09-original and C09-updated use the C09 scheme. The original Noah values of roughness lengths (z_{0m} = 0.12 m for grassland and z_{0m} = 0.1 m for bare soil) are used in Z95-original and C09-original, whereas Z95-updated and C09-updated use the revised z_{0m} values (z_{0m} = 0.035 m for grassland and z_{0m} = 0.011 m for bare soil) by Zheng et al. (2014). The values of z_{0m} used in Z95-original and C09-original for the Noah LSM are publicly available in the vegetation parameter table, which are described at the official Noah LSM website (http://www.ral.ucar.edu/research/land/technology/lsm.php).

5. Results

a. Impacts on T_{sfc} and surface energy budget modeling

The mean bias errors (MBEs) between the Noah LSM simulations at 1100 LST and the selected 312 daytime images of MOD11C1 T_{sfc} in the period 2005–10 are computed for the different roughness length parameterizations and for four seasons (Fig. 3). The histograms of the seasonal bias errors for grassland are depicted in Fig. 4. Figures 3 and 4 both show that Z95-original and C09-original generally underestimate the T_{sfc} in spring, autumn, and winter. Especially in winter, T_{sfc} is significantly underestimated in Z95-original and C09-original, with MBE of −7.6 K (Fig. 4m) and −6.8 K (Fig. 4o), respectively. These results are consistent with the previous finding that the Noah LSM tends to underestimate T_{sfc} during the daytime when applied to arid and semiarid regions (e.g., Hogue et al. 2005; Yang et al. 2009).

On average, Z95-updated reduces the MBEs relative to Z95-original by 2.7, 1.4, and 1.4 K for spring, autumn, and winter, whereas the MBE in summer has increased by 1.9 K. Similarly, C09-updated produces less MBE values (1.7, 2.3, and 0.8 K) than C09-original in spring, autumn, and winter, whereas larger MBE (4.3 K) is produced in summer. The use of Z95-updated and C09-updated has improved the spatial representativeness of the Noah LSM–simulated T_{sfc} in the relatively high-altitude regions, compared to the underestimated T_{sfc} values when using Z95-original and C09-original. The relationship between the elevation and the quality of the results on T_{sfc} will be discussed in section 6.

Table 2 lists the means μ and the standard deviations σ of H, R_{net}, LE, and G_0 simulated by the four experiments that correspond to the evaluated T_{sfc} during

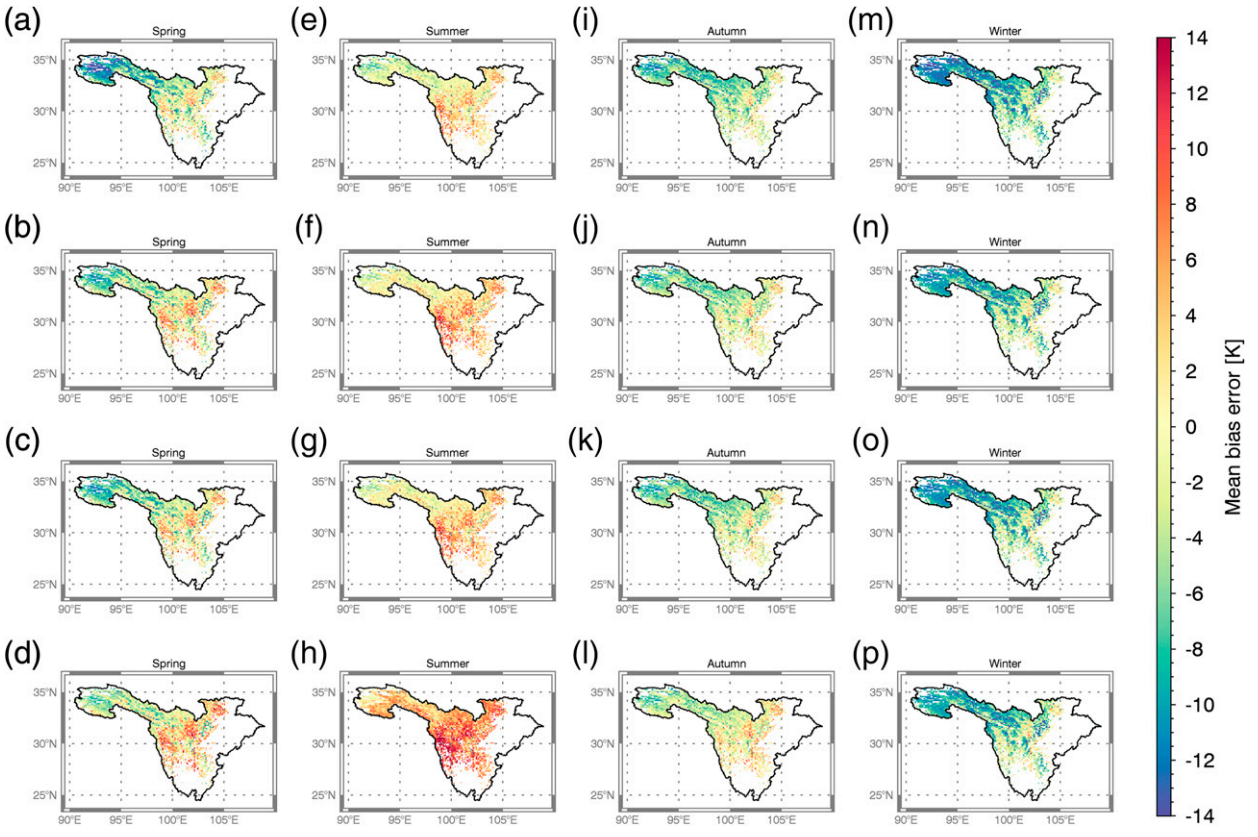

FIG. 3. The mean bias errors (K) of the Noah simulations at 1100 LST produced by (a),(e),(i),(m) Z95-original; (b),(f),(j),(n) Z95-updated; (c),(g),(k),(o) C09-original; and (d),(h),(l),(p) C09-updated during (a)–(d) spring, (e)–(h) summer, (i)–(l) autumn, and (m)–(p) winter based on 312 daytime images of MOD11C1 T_{sfc} products (~1030 LST) during the period 2005–10.

different seasons. The mean values of H from Z95-original and C09-original are respectively much larger than those from Z95-updated and C09-updated. In other words, Z95-updated and C09-updated notably reduce H values by ~21–56 W m^{-2} compared to Z95-original and C09-original for all seasons. The standard deviations of H indicate that the shapes for H distribution from Z95-updated and C09-updated become sharper and narrower than those of Z95-original and C09-original. As can also be seen from Table 2, Z95-updated and C09-updated produce averages of R_{net} that are respectively ~9–21 W m^{-2} lower than Z95-original and C09-original, whereas Z95-updated and C09-updated produce averages of G_0 that are ~14–37 W m^{-2} higher than Z95-original and C09-original. The mean values of LE produced by Z95-updated and C09-updated are very close to those simulated by Z95-original and C09-original, especially during spring and winter, and the differences between the H produced by the four experiments are notably larger than those between the LE and G_0. This is not surprising because in the dry season the conditions (e.g., soil moisture and temperature) for the production of latent heat are not favorable, and the available energy on the surface ($R_{net} - G_0$ or $H + LE$) is dominated by H (Chen et al. 2011).

b. *Impacts on water budget modeling*

The agreement between the simulations produced by numerical experiments and the observations is quantified using the following statistics: MBE, coefficient of determination R^2, root-mean-square error (RMSE), relative error (RE), and Nash–Sutcliffe model efficiency coefficient (NSE; Nash and Sutcliffe 1970). NSE is commonly used to quantitatively describe the accuracy of hydrological model outputs, with a range from $-\infty$ to 1, where the closer to 1, the more accurate the model prediction is (Moriasi et al. 2007).

Figure 5 compares the observed runoff with the simulation produced by all experiments. All designed experiments are capable of capturing the observed temporal pattern of the runoff, most notably the extreme drought in 2006. In comparison to measured values, the Noah LSM with Z95-original and C09-original systematically underestimated runoff, especially during the warm season (May–October).

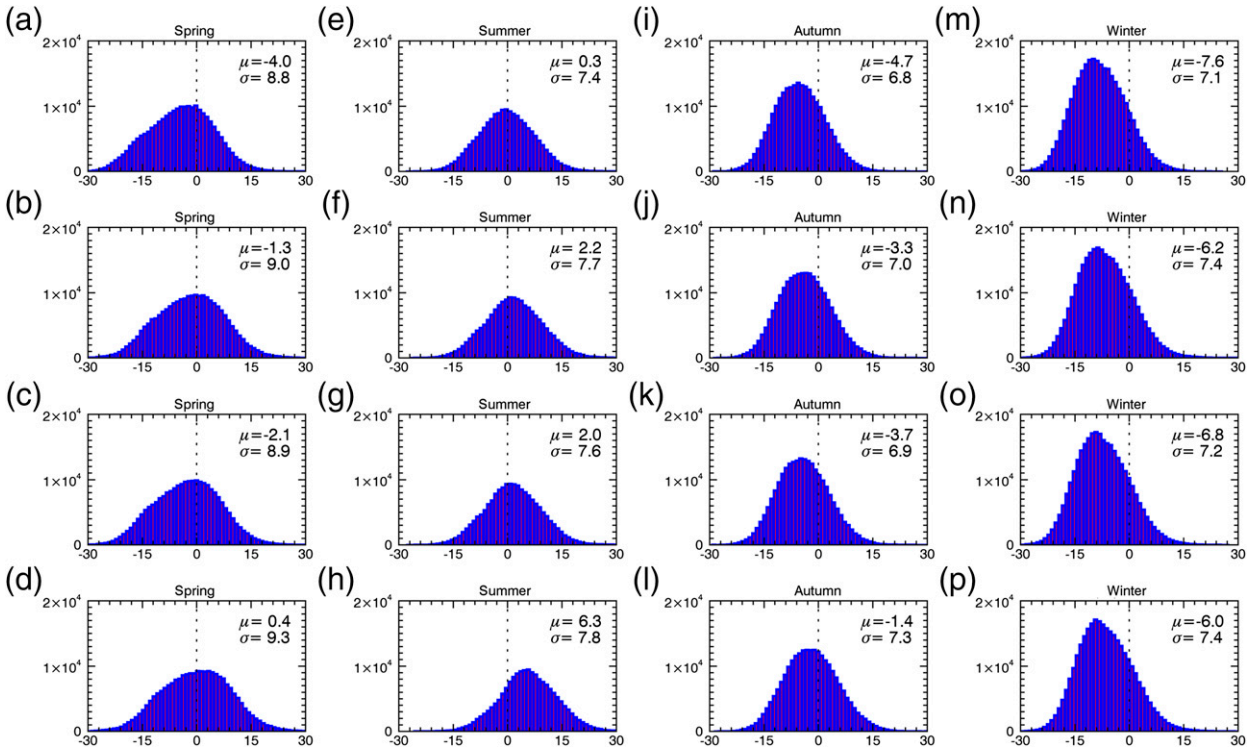

FIG. 4. The histograms of the bias errors (K) of the Noah simulations at 1100 LST produced by (a),(e),(i),(m) Z95-original; (b),(f),(j),(n) Z95-updated; (c),(g),(k),(o) C09-original; and (d),(h),(l),(p) C09-updated during (a)–(d) spring, (e)–(h) summer, (i)–(l) autumn, and (m)–(p) winter based on 312 daytime images of MOD11C1 T_{sfc} products (~1030 LST) during the period 2005–10.

However, as can be seen in Fig. 5 and Table 3, the Noah LSM with Z95-updated and C09-updated performs better on monthly runoff simulations than that with Z95-original and C09-original, respectively. We can also see from Fig. 5 that the Noah LSM using C09 performs better on monthly runoff simulations than using Z95. In terms of NSE, the runoff simulations of the Noah LSM can be improved by 26.3% and 19.0% with Z95-updated and C09-updated compared to Z95-original and C09-original, and the runoff results produced by C09-updated have 81.6%, 43.7%, and 19.0% improvement on that of Z95-original, Z95-updated, and C09-original, respectively. The results show that the selection of appropriate roughness length parameterizations improves the accuracy of runoff products of the Noah LSM.

We further verify the TWS anomalies simulated by the different experiments with the GRACE-observed TWS anomalies. As shown in Fig. 6a and Table 4, the seasonal variations of the TWS from Z95-updated and C09-updated better match GRACE-observed TWS variations than those obtained from Z95-original and C09-original in terms of NSE. Similar to runoff, the simulations of TWS anomalies are improved by implementing the scheme C09 in the Noah LSM in comparison with Z95. This further demonstrates the importance of adequate roughness length parameterizations for modeling the water budget.

6. Discussion

Equation (15) predicts that the values of z_{0m} and z_{0h} determine the surface exchange coefficient for heat transfer, which governs the total surface heat fluxes and affects T_{sfc} simulations. In the Z95 scheme, z_{0m} and C_{Zil} are set to constant values, whereas z_{0h} was described as a function of z_{0m} and atmospheric conditions (e.g., wind speed). On the other hand, the C09 scheme estimates z_{0m} as a function of GVF, and both C_{Zil} and z_{0h} vary with z_{0m}. This means that the dynamic of GVF greatly affects surface heat fluxes and T_{sfc} simulations when using the C09 scheme. The decrease of z_{0m} leads to the increase of C_{Zil}, which will further reduce z_{0h} and increase the heat transfer resistance, which is also shown in Table 5.

The differences between the C_h produced by the four experiments in Fig. 7 are consistent with that of the simulated T_{sfc} as shown in Figs. 3 and 4, and surface heat fluxes (H, R_{net}, LE, and G_0) as listed in Table 2. More specifically, the usage of Z95-original and C09-original in the Noah LSM generally underestimates T_{sfc} for alpine grasslands in the study area in spring, autumn, and

TABLE 2. Mean and std dev (W m^{-2}) of H, R_{net}, LE, and G_0 simulated by Z95-original, Z95-updated, C09-original, and C09-updated, which correspond to the evaluated T_{sfc} during different seasons.

	Spring		Summer		Autumn		Winter	
	μ	σ	μ	σ	μ	σ	μ	σ
H								
Z95-original	159	79	110	62	80	47	105	51
Z95-updated	103	60	89	50	55	33	59	36
C09-original	117	60	92	48	60	34	71	39
C09-updated	70	40	67	33	39	21	35	22
R_{net}								
Z95-original	399	127	450	135	288	121	221	79
Z95-updated	381	128	440	133	279	122	202	82
C09-original	387	127	442	133	281	122	208	81
C09-updated	371	125	421	128	272	117	191	79
LE								
Z95-original	66	62	197	84	87	66	16	19
Z95-updated	67	57	190	80	84	64	18	19
C09-original	70	58	194	81	88	64	20	20
C09-updated	71	51	175	72	81	57	24	19
G_0								
Z95-original	175	74	144	67	121	63	100	45
Z95-updated	212	90	164	74	140	70	125	60
C09-original	200	83	158	71	132	68	117	54
C09-updated	232	94	183	77	152	72	131	63

winter. This indicates that the coupling of heat from the grasslands to the atmosphere is too strong, that is, the values of C_h are overestimated. The overestimation of C_h will pump more H to heat the atmosphere and cool down the land surface. The end result of this cooling leads to lower upward longwave radiation (thus larger R_{net}) and a lower soil temperature gradient (thus lower G_0). On the other hand, using Z95-updated/C09-updated in the Noah LSM produces smaller values of C_h (Fig. 7) and therefore simulates higher T_{sfc} compared with using Z95-original/C09-original. As a result, the performance of the Noah LSM can be generally improved during spring, autumn, and winter. In contrast, using Z95-updated/C09-updated in the Noah LSM increases the warm biases in summer, when the T_{sfc} simulation results from the Noah LSM with Z95-original/C09-original match well with the T_{sfc} of MODIS.

The reason that the Noah LSM performs differently in summer is the distinct seasonal march of the surface water and energy budget in the central and eastern Tibetan Plateau. During the monsoon period (usually from June to September), the dry land surface becomes wet because of frequent rainfall events, and hence LE dominates the available energy on the surface ($R_{net} - G_0$ or H + LE) instead of H (Y08). This demonstrates that the Noah LSM with Z95-original/C09-original can perform well on T_{sfc} simulations for alpine grasslands during wet monsoon seasons, which is consistent with the assessment of the Noah LSM on the T_{sfc} simulations using observations on the Tibetan Plateau (Y08). This also implies that the schemes Z95 and C09 do not produce the seasonal variations of the T_{sfc} simulations on the Tibetan Plateau. We can also see from Figs. 3 and 4 that the Noah LSM using the C09 scheme generally performs better for grasslands than that using the

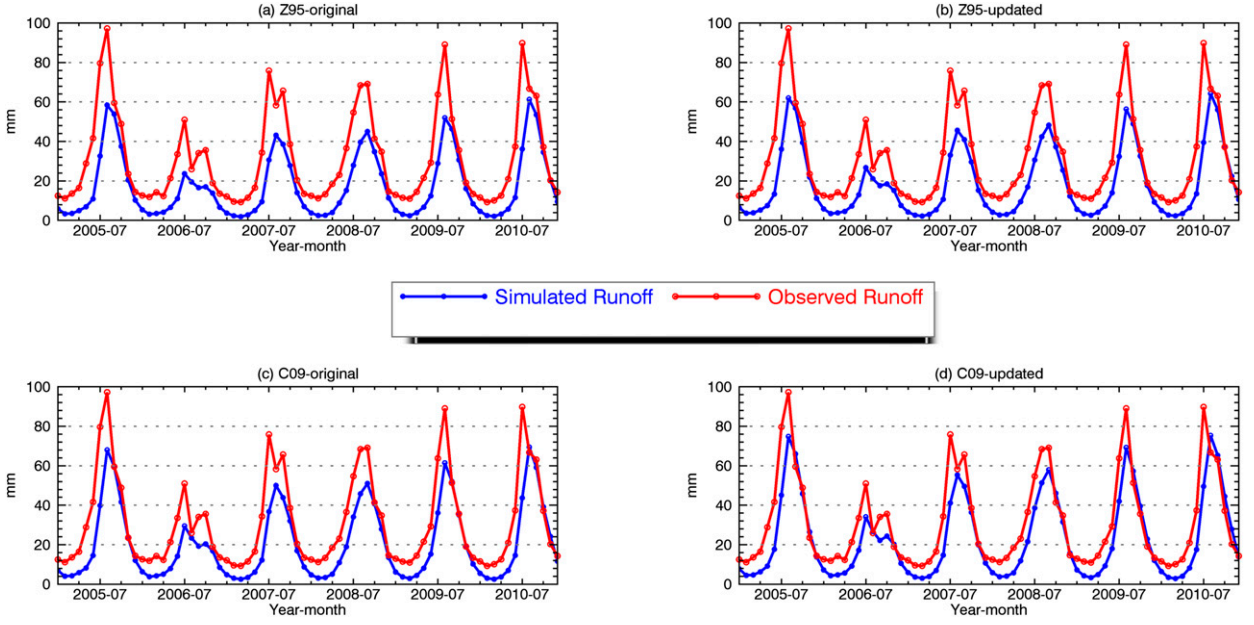

FIG. 5. Monthly time series of the observed and simulated runoff produced by (a) Z95-original, (b) Z95-updated, (c) C09-original, and (d) C09-updated during the period 2005–10.

TABLE 3. MBE, R^2, RMSE, RE, and NSE between the observed and estimated runoff produced by Z95-original, Z95-updated, C09-original, and C09-updated for the period 2005–10.

	MBE (mm month^{-1})	R^2	RMSE (mm month^{-1})	RE (mm month^{-1})	NSE
Z95-original	−14.12	0.79	18.09	−0.51	0.38
Z95-updated	−12.72	0.80	16.61	−0.47	0.48
C09-original	−11.06	0.82	14.96	−0.42	0.58
C09-updated	−8.34	0.83	12.75	−0.34	0.69

scheme Z95. This is because the scheme Z95 tends to largely underestimate the heat transfer resistances for short vegetation (grassland, crops, and shrub) in dry conditions (e.g., Chen et al. 2011), and relating C_h to the GVF dynamic can more realistically represent surface exchange processes in LSMs (C09).

As shown in Fig. 8, the Noah LSM with Z95-updated/C09-updated improves the T_{sfc} simulation performance in the relatively high-altitude regions (>4000 m), which may suggest a relation between the Noah LSM of T_{sfc} and the elevation. This relationship was also confirmed by, for instance, Salama et al. (2012). This dependency is mainly attributed to the fact that the climatology and land-cover conditions of the higher-altitude central Tibetan Plateau are different from the lower-elevation southeastern Tibetan Plateau (Fig. 1). More specifically, because of the large southeast–northwest precipitation gradient of the Tibetan Plateau (ranging from 100 to 700 mm in mean annual precipitation), the southeastern plateau is wetter than the central part (Y08). As a result, the distribution of the Tibetan grasslands is closely associated with the precipitation gradient across the

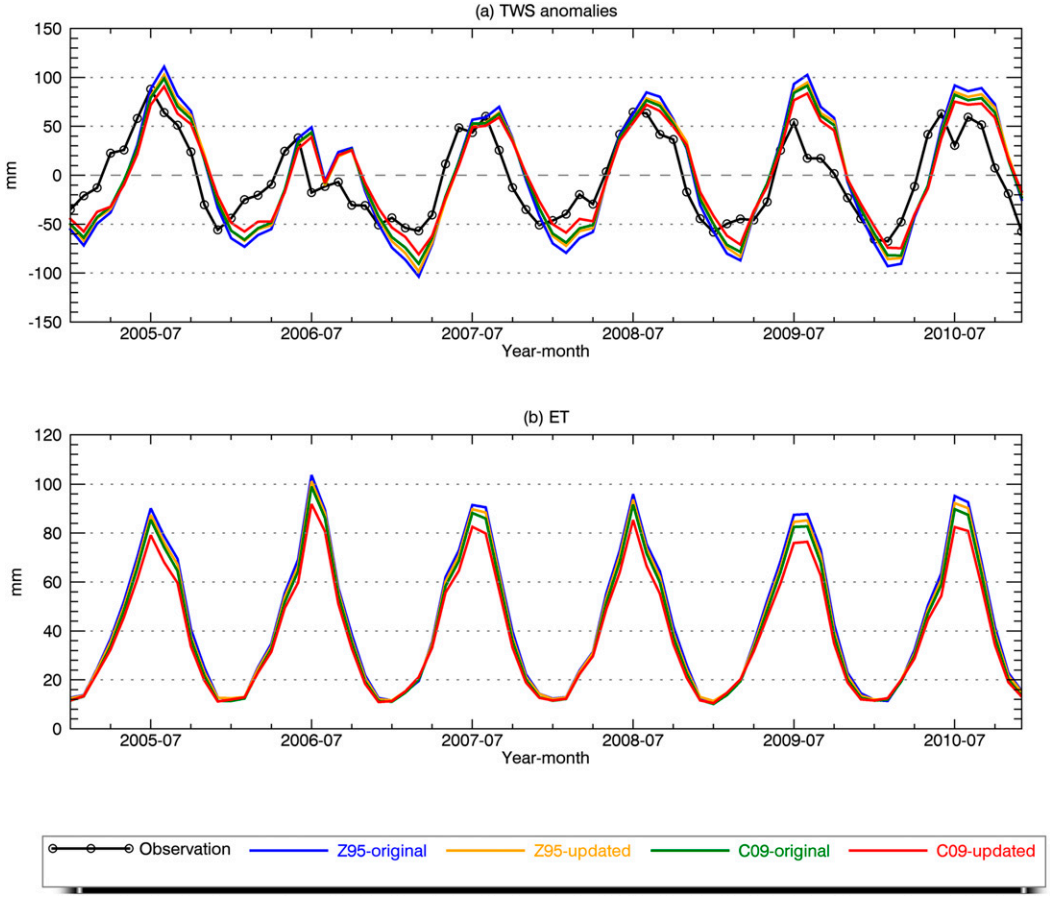

FIG. 6. Spatially averaged monthly time series of (a) GRACE-observed TWS anomalies (black) and (b) ET produced by Z95-original (blue), Z95-updated (orange), C09-original (green), and C09-updated (red) during the period 2005–10.

TABLE 4. MBE, R^2, RMSE, RE, and NSE between the GRACE-observed and estimated TWS anomalies produced by Z95-original, Z95-updated, C09-original, and C09-updated for the period 2005–10.

	MBE (mm month^{-1})	R^2	RMSE (mm month^{-1})	RE (mm month^{-1})	NSE
Z95-original	2.38	0.66	36.19	0.72	0.23
Z95-updated	3.01	0.63	33.91	0.57	0.32
C09-original	3.13	0.65	31.71	0.52	0.41
C09-updated	3.88	0.63	30.03	0.33	0.47

plateau. The central plateau mainly consists of semiarid steppe, whereas moist alpine meadow occurs in the relatively mesic southeastern plateau (Yang et al. 2010; Su et al. 2013). This further adds weight to the notion that the usage of Z95-updated and C09-updated is more suitable under dry conditions. It also indicates that the roughness length schemes Z95 and C09 have difficulties in estimating the reliable spatial distribution of daytime T_{sfc} for a region that has diverse climate and land surface conditions. Besides, this suggests that the vegetation types presented on the land surface in the Noah LSM should be further specified with respect to hydrometeorological conditions, and the roughness length parameterizations should be selected and, if needed, modified according to these specified vegetation types. The grassland on the Tibetan Plateau, for instance, can be classified into arid alpine steppe, semiarid alpine steppe, moist alpine meadows, etc.

The standard deviations of the four experiments for the same season (shown in Fig. 4) are very close, indicating that changing the roughness lengths only changes MBE without affecting the shape of the probability distribution of the errors. On the one hand, it means that the MBE can be used as the single indicator for the evaluation of the simulated T_{sfc}. On the other hand, our results show that it is possible to model the probability distribution of the errors between Noah simulation and MODIS satellite observation, which can be used for data assimilation.

Besides T_{sfc} and surface heat fluxes simulations, the roughness length parameterizations have large effects on the simulations of the water budget components. As described in section 5, Z95-updated/C09-updated improves the monthly runoff and TWS simulations (Figs. 5, 6), which indicates that a more realistic representation of the heat transfer resistance can increase the Noah LSM simulation accuracy of the water fluxes and states. The improvement in runoff simulation is attributed to the increased amount of monthly runoff (Fig. 5, Table 3), predominantly the increase of base flow (Fig. 9).

The fact that the Noah LSM with Z95-updated/C09-updated increases the monthly amount of base flow and benefits the TWS anomalies can be explained as follows. The higher T_{sfc} simulated by the Noah LSM with Z95-updated/C09-updated, due to the decreased C_q, will reduce the R_{net} [Eq. (1)], lead to more G_0 by raising the ground-soil temperature gradient [Eq. (8)], and consequently reduce the LE_P [Eq. (4)]. Moreover, the lower z_{0m} means decreased C_q [Eq. (15)], which will weaken the land–atmosphere coupling strength for water vapor transfer and reduce the LE_P [Eq. (4)]. This decreased LE_P could reduce the actual ET [Eqs. (5)–(7)], which is consistent with (as shown in Fig. 6b) the ET results of Z95-updated/C09-updated during the warm season being lower than that of Z95-original/C09-original. As ET decreases, less water is extracted from soil for ET and more water is retained in the soil columns. As a result, the soil moisture of Z95-updated/C09-updated is higher than that of Z95-original/C09-original. The increased soil moisture favors the runoff generation, leading to an improved runoff simulation for Z95-updated/C09-updated. More specifically, the increased liquid soil moisture raises hydraulic conductivity (Campbell 1974) and increases the soil drainage, leading to more baseflow generation [Eq. (12)].

On the other hand, we can see from Fig. 9a that the increased soil moisture content has a minor effect on the simulated surface runoff. This can be attributed to

TABLE 5. Averaged z_{0m}, z_{0h}, and C_{Zil} produced by Z95-original, Z95-updated, C09-original, and C09-updated, which correspond to the evaluated T_{sfc} during different seasons.

	Spring			Summer			Autumn			Winter		
	z_{0m}	z_{0h}	C_{Zil}	z_{0m}	z_{0h}	C_{Zil}	z_{0m}	z_{0h}	C_{Zil}	z_{0m}	z_{0h}	C_{Zil}
Z95-original	0.120	0.101	0.100	0.120	0.116	0.100	0.120	0.107	0.100	0.120	0.100	0.100
Z95-updated	0.035	0.013	0.100	0.035	0.030	0.100	0.035	0.020	0.100	0.035	0.012	0.100
C09-original	0.102	0.101	0.261	0.102	0.101	0.261	0.108	0.107	0.241	0.101	0.099	0.263
C09-updated	0.013	0.013	0.838	0.030	0.030	0.674	0.021	0.020	0.763	0.013	0.012	0.845

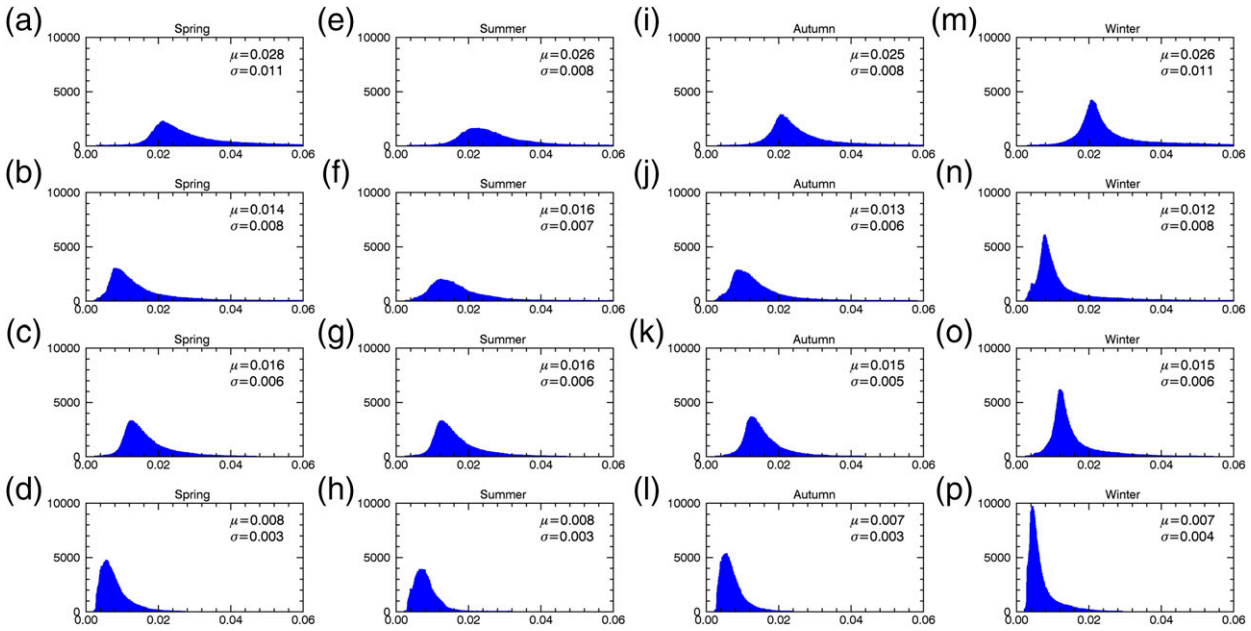

FIG. 7. The histograms of C_h corresponding to the evaluated T_{sfc} simulated by (a),(e),(i),(m) Z95-original; (b),(f),(j),(n) Z95-updated; (c),(g),(k),(o) C09-original; and (d),(h),(l),(p) C09-updated during (a)–(d) spring, (e)–(h) summer, (i)–(l) autumn, and (m)–(p) winter.

the fact that the moisture deficits in the soil columns are usually small during the wet monsoon period (Schaake et al. 1996), and hence, the maximum infiltration capacities calculated based on Eq. (10) for the four experiments are very close. Consequently, the surface runoff simulation, which is determined by the rain intensity and the maximum infiltration capacity as shown in Eq. (9), does not vary largely. Likewise, the difference between the amounts of runoff from Z95 and from C09 is attributed to the difference between the values of C_h (C_q) from Z95 and from C09. This demonstrates that the roughness length parameterizations, which determine C_h and C_q, play an important role in controlling the total amount of runoff in the LSM simulation for high-altitude catchments.

It should be noted that the improvement in runoff simulation mainly occurs in the warm season (May–October). This is because, during the cold season (November–April), the production of LE is very low because of the limitations of, for instance, soil moisture and temperature, and therefore the roughness lengths have a negligible effect on the ET simulation. It should be noted that snow cover is limited because of strong wind and little precipitation in the study area during the cold season (Malik et al. 2014), and hence the runoff production is little influenced by the snowpack. Moreover, it may be unfair to compare the Noah LSM–simulated runoff directly (without river routing) with the discharge at the gauging station. However, we compare the runoff with the observation at a monthly scale rather than an hourly or a daily scale; thus, the influence of the river routing on the comparison is minor, which is supported by Yang et al. (2011) and Cai et al. (2014).

Although Z95-updated/C09-updated improves the Noah LSM simulations, T_{sfc} and monthly runoff are still largely underestimated. This can be explained by the following reasons. The first one is the imperfect roughness length schemes for high-altitude regions under frozen soil conditions. When the water in the soil is frozen, the land surfaces tend to be smoother (Zheng et al. 2014). As such, the values of z_{0h} and z_{0m} are still overestimated within the Noah LSM, leading to only a slight improvement in T_{sfc} simulation for the winter period, even when using the Z95-updated/C09-updated parameterizations (Figs. 3, 4).

The second explanation forms the inherent uncertainties associated with the simulation of the soil water flow and heat transport and their impact on the computed surface energy and water budgets. For instance, Yang et al. (2005, 2009) and Chen et al. (2013) have demonstrated that the absence of vertical soil heterogeneity in the model structure causes difficulties in the simulation of soil moisture and temperature profiles across the Tibetan Plateau by the Noah LSM. Furthermore, Su et al. (2013) pointed out that the simulation of freeze–thaw transitions in the soil play an important role in reliability of the modeled soil moisture and temperature profiles. In addition, the soil column adopted by the Noah LSM has only a 2-m depth, and a

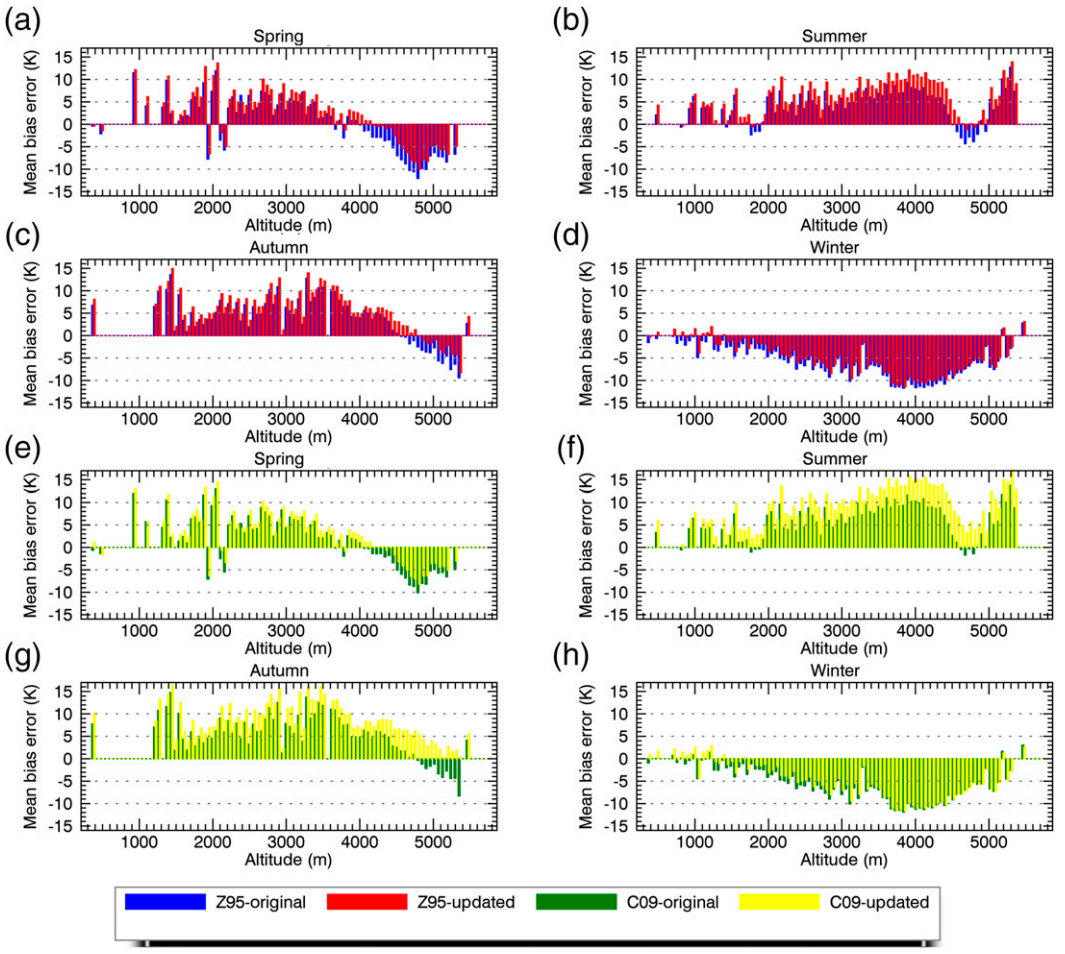

FIG. 8. The mean bias errors (K) of the Noah simulations for different altitudes at 1100 LST produced by Z95-original (blue), Z95-updated (red), C09-original (green), and C09-updated (yellow) during (a),(e) spring; (b),(f) summer; (c),(g) autumn; and (d),(h) winter based on 312 daytime images of MOD11C1 T_{sfc} products (~1030 LST) during the period 2005–10.

free gravitational drainage is employed for the baseflow production. The disadvantage of this setup is the inability to redistribute water across the soil column via the capillary rise and deeper layers including groundwater (Gulden et al. 2007; Niu et al. 2011). This can lead to drier soils and, consequently, an underestimation of the runoff as Niu et al. (2005) and Yang et al. (2011) have previously reported.

The third reason is the forcing data. Inaccuracies existing in the forcing data may have substantial impacts on the land surface simulations. Chen et al. (2011) compared the daily averaged radiation fluxes of ITPCAS forcing data against those from field measurements at four dryland sites on the Tibetan Plateau, and the results show that the ITPCAS data are dramatically improved in terms of radiation in comparison with the widely used GLDAS dataset; however, the daily averaged longwave radiation of the ITPCAS forcing data is still notably underestimated. More specifically, Chen et al. (2011, their Table 4) gives the statistical metrics (R^2, MBE, and RMSE) for daily averaged ITPCAS radiation fluxes against the observed data at four sites (Amdo, Gaize, Dunhuang, and Tongyu) on the Tibetan Plateau during 2003–04. They show that the MBEs of the daily averaged longwave radiation fluxes of the ITPCAS forcing data are mostly negative and up to $-23.4\,\mathrm{W\,m^{-2}}$. As incoming radiation fluxes play a key role for simulating surface energy partitioning and T_{sfc}, the underestimated incoming radiation can be one of the reasons that cause the underestimation of T_{sfc}.

7. Conclusions

In this paper, we have addressed the regional-scale effects of the roughness length parameterizations for grasslands on the Tibetan Plateau in the Noah LSM.

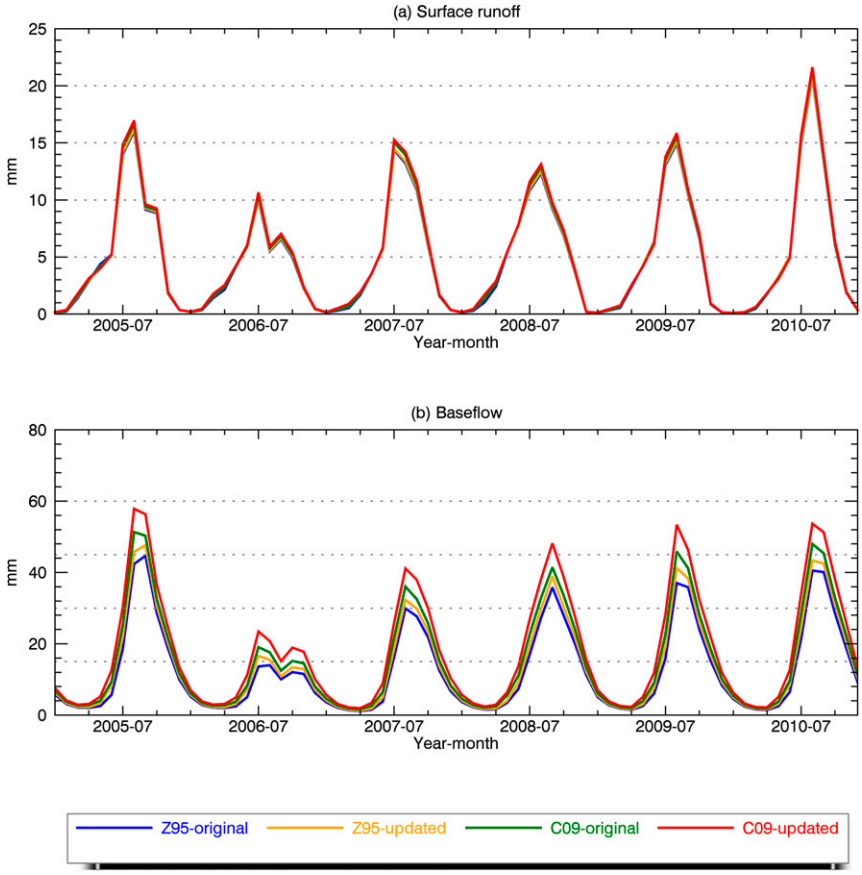

FIG. 9. Monthly time series of (a) surface runoff and (b) base flow produced by Z95-original (blue), Z95-updated (orange), C09-original (green), and C09-updated (red) during the period 2005–10.

Four numerical experiments with two different roughness schemes were conducted during the period 2005–10 for the high-altitude hydrological catchment, the source region of the Yangtze basin in China. The experimental setups were based on physical process knowledge, verified with various satellite products, and validated with ground-based observations. This study highlights the need for regional adaptation of the z_{0m} and z_{0h} values and provides insight into the regional-scale land surface modeling of high-altitude catchments. The main findings of this work are listed as follows:

1) The usage of Z95-updated/C09-updated improves, validated by the MODIS products, the regional-scale predictions of the Noah LSM with Z95-original/C09-original on T_{sfc} for a high-altitude basin in spring, autumn, and winter, but larger warm biases are produced in summer. This implies that the roughness length schemes Z95 and C09 cannot satisfactorily capture the seasonal variations of the T_{sfc} simulations on the Tibetan Plateau, and Z95-updated and C09-updated are more suitable in relatively dry conditions.
2) Z95-updated/C09-updated improves the T_{sfc} simulation performance in the relatively high-altitude regions (>4000 m), whereas larger warm biases are produced in low-altitude regions of the Tibetan Plateau. This indicates that the roughness length schemes Z95 and C09 have difficulties in estimating the reliable spatial distribution of daytime T_{sfc} for a region that has diverse climate and land surface conditions. One feasible way to address this issue is the grasslands on the Tibetan Plateau are further classified into arid alpine steppe, semiarid alpine steppe, moist alpine meadows, etc., and the roughness length parameterizations are selected and, if needed, modified according to these further specified vegetation types.
3) The Noah LSM with Z95-original/C09-original largely underestimates the monthly runoff in the source region of the Yangtze River. However, by implementing Z95-updated/C09-updated, the monthly amount of runoff can be largely increased. Also, Z95-updated/C09-updated increases the agreement of the Noah TWS simulation with the GRACE-derived TWS.

This demonstrates that the roughness length parameterization, in association with surface exchange coefficient for heat C_h and moisture C_q transfer, plays an important role in modeling water budget components for high-altitude catchments.

4) The Noah LSM using the scheme C09 generally performs better than that using the scheme Z95 on the simulations of regional-scale T_{sfc} and water budget components. It is therefore recommended to use C09-updated for LSM simulations in the central and eastern part of the Tibetan Plateau, particularly in dry conditions.

Acknowledgments. This research was funded in part by the ESA-MOST Dragon III Programme: Concerted Earth Observation and Prediction of Water and Energy Cycles in the Third Pole Environment (CEOPTPE). Ying Huang was supported by the Chinese Scholarship Council (CSC). We are grateful to the editor and reviewers for their valuable comments and constructive suggestions, which have greatly assisted us in improving the quality of the paper. Moreover, we thank all the researchers who processed the atmospheric forcing data provided by the Institute of Tibetan Plateau Research, Chinese Academy of Sciences (ITPCAS); the Cuntan discharge observations provided by Bureau of Hydrology, Changjiang Water Resources Commission; the Moderate Resolution Imaging Spectroradiometer (MODIS) product provided by U.S. Geological Survey (USGS), and the RL05 GRACE L2 product provided by the Center for Space Research (CSR) at the University of Texas at Austin and Jet Propulsion Laboratory (JPL), NASA, United States.

REFERENCES

Balsamo, G., A. Beljaars, K. Scipal, P. Viterbo, B. van den Hurk, M. Hirschi, and A. K. Betts, 2009: A revised hydrology for the ECMWF model: Verification from field site to terrestrial water storage and impact in the integrated forecast system. *J. Hydrometeor.*, **10**, 623–643, doi:10.1175/2008JHM1068.1.

Brutsaert, W., 1982: *Evaporation into the Atmosphere: Theory, History and Applications*. Springer, 319 pp.

——, 1998: Land-surface water vapor and sensible heat flux: Spatial variability, homogeneity, and measurement scales. *Water Resour. Res.*, **34**, 2433–2442, doi:10.1029/98WR01340.

Cai, X., Z.-L. Yang, C. H. David, G.-Y. Niu, and M. Rodell, 2014: Hydrological evaluation of the Noah-MP land surface model for the Mississippi River basin. *J. Geophys. Res. Atmos.*, **119**, 23–38, doi:10.1002/2013JD020792.

Campbell, G. S., 1974: A simple method for determining unsaturated conductivity from moisture retention data. *Soil Sci.*, **117**, 311–314, doi:10.1097/00010694-197406000-00001.

Chen, F., and Y. Zhang, 2009: On the coupling strength between the land surface and the atmosphere: From viewpoint of surface exchange coefficients. *Geophys. Res. Lett.*, **36**, L10404, doi:10.1029/2009GL037980.

——, Z. Janjić, and K. Mitchell, 1997: Impact of atmospheric surface-layer parameterizations in the new land-surface scheme of the NCEP mesoscale Eta model. *Bound.-Layer Meteor.*, **85**, 391–421, doi:10.1023/A:1000531001463.

Chen, L., and O. W. Frauenfeld, 2014: Surface air temperature changes over the twentieth and twenty-first centuries in China simulated by 20 CMIP5 models. *J. Climate*, **27**, 3920–3937, doi:10.1175/JCLI-D-13-00465.1.

Chen, Y., K. Yang, D. Zhou, J. Qin, and X. Guo, 2010: Improving the Noah land surface model in arid regions with an appropriate parameterization of the thermal roughness length. *J. Hydrometeor.*, **11**, 995–1006, doi:10.1175/2010JHM1185.1.

——, ——, J. He, J. Qin, J. Shi, J. Du, and Q. He, 2011: Improving land surface temperature modeling for dry land of China. *J. Geophys. Res.*, **116**, D20104, doi:10.1029/2011JD015921.

——, ——, J. Qin, L. Zhao, W. Tang, and M. Han, 2013: Evaluation of AMSR-E retrievals and GLDAS simulations against observations of a soil moisture network on the central Tibetan Plateau. *J. Geophys. Res. Atmos.*, **118**, 4466–4475, doi:10.1002/jgrd.50301.

Crawford, T. M., and C. E. Duchon, 1999: An improved parameterization for estimating effective atmospheric emissivity for use in calculating daytime downwelling longwave radiation. *J. Appl. Meteor.*, **38**, 474–480, doi:10.1175/1520-0450(1999)038<0474:AIPFEE>2.0.CO;2.

Dirmeyer, P. A., R. D. Koster, and Z. Guo, 2006: Do global models properly represent the feedback between land and atmosphere? *J. Hydrometeor.*, **7**, 1177–1198, doi:10.1175/JHM532.1.

Fu, C. B., and G. Wen, 2002: Several issues on aridification in the northern China (in Chinese). *Climatic Environ. Res.*, **7**, 22–29.

Garratt, J. R., 1994: *The Atmospheric Boundary Layer*. Cambridge University Press, 336 pp.

Gulden, L. E., E. Rosero, Z.-L. Yang, M. Rodell, C. S. Jackson, G.-Y. Niu, P. J.-F. Yeh, and J. Famiglietti, 2007: Improving land-surface model hydrology: Is an explicit aquifer model better than a deeper soil profile? *Geophys. Res. Lett.*, **34**, L09402, doi:10.1029/2007GL029804.

He, J., and K. Yang, 2011: China meteorological forcing dataset. Cold and Arid Regions Science Data Center at Lanzhou, accessed 4 March 2016, doi:10.3972/westdc.002.2014.db.

Hogue, T. S., L. Bastidas, H. Gupta, S. Sorooshian, K. Mitchell, and W. Emmerich, 2005: Evaluation and transferability of the Noah land surface model in semiarid environments. *J. Hydrometeor.*, **6**, 68–84, doi:10.1175/JHM-402.1.

Huffman, G. J., and Coauthors, 2007: The TRMM Multisatellite Precipitation Analysis (TMPA): Quasi-global, multiyear, combined-sensor precipitation estimates at fine scales. *J. Hydrometeor.*, **8**, 38–55, doi:10.1175/JHM560.1.

Immerzeel, W. W., L. P. H. van Beek, and M. F. P. Bierkens, 2010: Climate change will affect the Asian water towers. *Science*, **328**, 1382–1385, doi:10.1126/science.1183188.

Koike, T., 2004: The Coordinated Enhanced Observing Period: An initial step for integrated global water cycle observation. *WMO Bull.*, **53**, 115–121.

Landerer, F. W., and S. C. Swenson, 2012: Accuracy of scaled GRACE terrestrial water storage estimates. *Water Resour. Res.*, **48**, W04531, doi:10.1029/2011WR011453.

LeMone, M. A., M. Tewari, F. Chen, J. G. Alfieri, and D. Niyogi, 2008: Evaluation of the Noah land surface model using data from a fair-weather IHOP 2002 day with heterogeneous surface fluxes. *Mon. Wea. Rev.*, **136**, 4915–4941, doi:10.1175/2008MWR2354.1.

LPDAAC, 2001: The MODIS/Terra LST/E Daily L3 Global 0.05Deg CMG, Version 4-5.5. NASA EOSDIS Land Processes DAAC, accessed 6 March 2014, doi:10.5067/ASTER/AST_L1B.003.

Ma, Y., O. Tsukamoto, J. Wang, H. Ishikawa, and I. Tamagawa, 2002: Analysis of aerodynamic and thermodynamic parameters on the grassy marshland surface of Tibetan Plateau. *Prog. Nat. Sci.*, **12**, 36–40.

——, M. Menenti, R. Feddes, and J. Wang, 2008: Analysis of the land surface heterogeneity and its impact on atmospheric variables and the aerodynamic and thermodynamic roughness lengths. *J. Geophys. Res.*, **113**, D08113, doi:10.1029/2007JD009124.

Ma, Z., and C. Fu, 2006: Some evidence of drying trend over northern China from 1951 to 2004. *Chinese Sci. Bull.*, **51**, 2913–2925, doi:10.1007/s11434-006-2159-0.

Mahrt, L., and M. Ek, 1984: The influence of atmospheric stability on potential evaporation. *J. Climate Appl. Meteor.*, **23**, 222–234, doi:10.1175/1520-0450(1984)023<0222:TIOASO>2.0.CO;2.

——, and H. Pan, 1984: A two-layer model of soil hydrology. *Bound.-Layer Meteor.*, **29**, 1–20, doi:10.1007/BF00119116.

Malik, M. J., R. van der Velde, Z. Vekerdy, and Z. Su, 2014: Improving modeled snow albedo estimates during the spring melt season. *J. Geophys. Res. Atmos.*, **119**, 7311–7331, doi:10.1002/2013JD021344.

Martano, P., 2000: Estimation of surface roughness length and displacement height from single-level sonic anemometer data. *J. Appl. Meteor.*, **39**, 708–715, doi:10.1175/1520-0450(2000)039<0708:EOSRLA>2.0.CO;2.

Moriasi, D. N., J. G. Arnold, M. W. Van Liew, R. L. Bingner, R. D. Harmel, and T. L. Veith, 2007: Model evaluation guidelines for systematic quantification of accuracy in watershed simulations. *Trans. Amer. Soc. Agric. Biol. Eng.*, **50**, 885–900, doi:10.13031/2013.23153.

Nash, J. E., and J. V. Sutcliffe, 1970: River flow forecasting through conceptual models part I—A discussion of principles. *J. Hydrol.*, **10**, 282–290, doi:10.1016/0022-1694(70)90255-6.

Niu, G.-Y., Z.-L. Yang, R. E. Dickinson, and L. E. Gulden, 2005: A simple TOPMODEL-based runoff parameterization (SIMTOP) for use in global climate models. *J. Geophys. Res.*, **110**, D21106, doi:10.1029/2005JD006111.

——, and Coauthors, 2011: The community Noah land surface model with multiparameterization options (Noah-MP): 1. Model description and evaluation with local-scale measurements. *J. Geophys. Res.*, **116**, D12109, doi:10.1029/2010JD015139.

Salama, M. S., R. Van der Velde, L. Zhong, Y. Ma, M. Ofwono, and Z. Su, 2012: Decadal variations of land surface temperature anomalies observed over the Tibetan Plateau by the Special Sensor Microwave Imager (SSM/I) from 1987 to 2008. *Climatic Change*, **114**, 769–781, doi:10.1007/s10584-012-0427-3.

Schaake, J. C., V. I. Koren, Q.-Y. Duan, K. Mitchell, and F. Chen, 1996: Simple water balance model for estimating runoff at different spatial and temporal scales. *J. Geophys. Res.*, **101**, 7461–7475, doi:10.1029/95JD02892.

Sheffield, J., G. Goteti, and E. F. Wood, 2006: Development of a 50-year high-resolution global dataset of meteorological forcings for land surface modeling. *J. Climate*, **19**, 3088–3111, doi:10.1175/JCLI3790.1.

Su, Z., T. Schmugge, W. P. Kustas, and W. J. Massman, 2001: An evaluation of two models for estimation of the roughness height for heat transfer between the land surface and the atmosphere. *J. Appl. Meteor.*, **40**, 1933–1951, doi:10.1175/1520-0450(2001)040<1933:AEOTMF>2.0.CO;2.

——, P. de Rosnay, J. Wen, L. Wang, and Y. Zeng, 2013: Evaluation of ECMWF's soil moisture analyses using observations on the Tibetan Plateau. *J. Geophys. Res. Atmos.*, **118**, 5304–5318, doi:10.1002/jgrd.50468.

Sun, J., 1999: Diurnal variations of thermal roughness height over a grassland. *Bound.-Layer Meteor.*, **92**, 407–427, doi:10.1023/A:1002071421362.

Swenson, S. C., 2012: GRACE monthly land water mass grids NETCDF release 5.0, Ver. 5.0. PO.DAAC, accessed 6 January 2014, doi:10.5067/TELND-NC005.

——, and J. Wahr, 2006: Post-processing removal of correlated errors in GRACE data. *Geophys. Res. Lett.*, **33**, L08402, doi:10.1029/2005GL025285.

Xu, X., and Coauthors, 2008: A new integrated observational system over the Tibetan Plateau. *Bull. Amer. Meteor. Soc.*, **89**, 1492–1496, doi:10.1175/2008BAMS2557.1.

Yanai, M., and G.-X. Wu, 2006: Effects of the Tibetan Plateau. *The Asian Monsoon*, Springer, 513–549.

——, C. Li, and Z. Song, 1992: Seasonal heating of the Tibetan Plateau and its effects on the evolution of the Asian summer monsoon. *J. Meteor. Soc. Japan*, **70**, 319–351.

Yang, K., T. Koike, and D. Yang, 2003: Surface flux parameterization in the Tibetan Plateau. *Bound.-Layer Meteor.*, **106**, 245–262, doi:10.1023/A:1021152407334.

——, ——, B. Ye, and L. Bastidas, 2005: Inverse analysis of the role of soil vertical heterogeneity in controlling surface soil state and energy partition. *J. Geophys. Res.*, **110**, D08101, doi:10.1029/2004JD005500.

——, ——, and ——, 2006: Improving estimation of hourly, daily, and monthly solar radiation by importing global data sets. *Agric. For. Meteor.*, **137**, 43–55, doi:10.1016/j.agrformet.2006.02.001.

——, and Coauthors, 2007: Initial CEOP-based review of prediction skill of operational general circulation models and land surface models. *J. Meteor. Soc. Japan*, **85A**, 99–116.

——, and Coauthors, 2008: Turbulent flux transfer over bare-soil surfaces: Characteristics and parameterization. *J. Appl. Meteor. Climatol.*, **47**, 276–290, doi:10.1175/2007JAMC1547.1.

——, Y. Y. Chen, and J. Qin, 2009: Some practical notes on the land surface modeling in the Tibetan Plateau. *Hydrol. Earth Syst. Sci.*, **13**, 687–701, doi:10.5194/hess-13-687-2009.

Yang, S. L., and Coauthors, 2010: Temporal variations in water resources in the Yangtze River (Changjiang) over the Industrial Period based on reconstruction of missing monthly discharges. *Water Resour. Res.*, **46**, W10516, doi:10.1029/2009WR008589.

Yang, Z.-L., and Coauthors, 2011: The community Noah land surface model with multiparameterization options (Noah-MP): 2. Evaluation over global river basins. *J. Geophys. Res.*, **116**, D12110, doi:10.1029/2010JD015140.

Zhang, J., L. Wu, and W. Dong, 2011: Land–atmosphere coupling and summer climate variability over East Asia. *J. Geophys. Res.*, **116**, D05117, doi:10.1029/2010JD014714.

Zheng, D., R. Van Der Velde, Z. Su, M. J. Booij, and A. Y. Hoekstra, 2014: Assessment of roughness length schemes implemented within the Noah land surface model for high-altitude regions. *J. Hydrometeor.*, **15**, 921–937, doi:10.1175/JHM-D-13-0102.1.

Zheng, W., H. Wei, Z. Wang, X. Zeng, J. Meng, M. Ek, K. Mitchell, and J. Derber, 2012: Improvement of daytime land surface skin temperature over arid regions in the NCEP GFS model and its impact on satellite data assimilation. *J. Geophys. Res.*, **117**, D06117, doi:10.1029/2011JD015901.

Zilitinkevich, S. S., 1995: Non-local turbulent transport: Pollution dispersion aspects of coherent structure of convective flows. *Air Pollution Theory and Simulation*, Vol. 1, *Air Pollution III*, edited by H. Power, N. Moussiopoulos, and C. A. Brebbia, Computational Mechanics Publications, 53–60.